Surface Deformation Surrounding the 2021 $M_{\rm w}$ 7.2 Haiti Earthquake Illuminated by InSAR Observations

Harriet Zoe Yin^{*1}, Xiaohua Xu², Jennifer S. Haase¹, Roby Douilly³, David T. Sandwell¹, and Bernard Mercier de Lepinay⁴

ABSTRACT

Earthquakes pose a major threat to the people of Haiti, as tragically shown by the catastrophic 2010 $M_{\rm w}$ 7.0 earthquake and more recently by the 2021 $M_{\rm w}$ 7.2 earthquake. Both events occurred within the transpressional Enriquillo-Plantain Garden fault zone (EPGFZ), which runs through the southern peninsula of Haiti and is a major source of seismic hazard for the region. Satellite-based Interferometric Synthetic Aperture Radar (InSAR) data are used to illuminate the ground deformation patterns associated with the 2021 event. The analysis of Sentinel-1 and Advanced Land Observation Satellite (ALOS)-2 InSAR data shows (1) the broad coseismic deformation field; (2) detailed secondary fault structures as far as 12 km from the main Enriquillo-Plantain Garden fault (EPGF), which are active during and after the earthquake; and (3) postseismic shallow slip, which migrates along an ~ 40 km unruptured section of the EPGF for approximately two weeks following the earthquake. The involvement of secondary faults in this rupture requires adjustments to the representation of hazard that assumes a simple segmented strike-slip EPGF. This work presents the first successful use of phase gradient techniques to map postseismic deformation in a vegetated region, which opens the door to future studies of a larger number of events in a wider variety of climates.

KEY POINTS

- InSAR data are used to create detailed surface deformation maps of the 2021 $M_{\rm w}$ 7.2 Haiti earthquake.
- InSAR phase gradients reveal postseismic slip at the edges of the rupture and slip on secondary faults.
- The slip on secondary faults indicates that some geologic structures were reactivated by the earthquake.

Supplemental Material

INTRODUCTION

The Enriquillo-Plantain Garden fault zone (EPGFZ) accommodates roughly half of the 20 mm/year of relative motion between the Caribbean plate and the North American plate (DeMets et al., 2000), as the margin transitions from transform motion in the western Caribbean to subduction in the Antilles arc (Mann et al., 1995). Recent geodetic studies have shown slip rates of 9-10 mm/yr along the EPGFZ on the southern peninsula of Haiti with a largely left-lateral orientation and some compressional motion (Symithe et al., 2015; Symithe and Calais, 2016). There has been a recognized need to understand strain partitioning in this transpressional boundary following geodetic studies illustrating the interaction of offshore and onshore thrust systems with the main strike-slip strand of the fault zone, the EPGF, during the holocene (Wang et al., 2018). The geology and faults of the EPGFZ have been mapped in detail (Boisson, 1987; Bien-Aime-Momplaisir et al., 1988), and more recent work has reexamined these maps to interpret the major active faults and their segmentation (Prentice et al., 2010; Wessels et al., 2019; Saint Fleur et al., 2020), which could be hypothesized to constrain the length of characteristic earthquake ruptures. The current seismic hazard maps constructed for Haiti were a major improvement over the previous global hazard maps (Frankel et al., 2011).

Cite this article as Zoe Yin, H., X. Xu, J. S. Haase, R. Douilly, D. T. Sandwell, and B. Mercier de Lepinay (2022). Surface Deformation Surrounding the 2021 $M_{\rm w}$ 7.2 Haiti Earthquake Illuminated by InSAR Observations, Bull. Seismol. Soc. Am. 113, 41-57, doi: 10.1785/0120220109

© Seismological Society of America

^{1.} Scripps Institution of Oceanography, UCSD, La Jolla, California, U.S.A., https:// (JSH); https://orcid.org/0000-0001-5657-8707 (DTS); 2. University of Texas Institute for Geophysics, Austin, Texas, U.S.A., (b) https://orcid.org/0000-0002-1213-3017 (XX); 3. University of California, Riverside, California, U.S.A., https://orcid.org/ 0000-0003-1724-2535 (RD); 4. Centre National de la Recherche Scientifique, GéoAzur, Université Côte d'Azur, Valbonne, France, https://orcid.org/0000-0002-9804-943X (BML)

^{*}Corresponding author: hyin@ucsd.edu

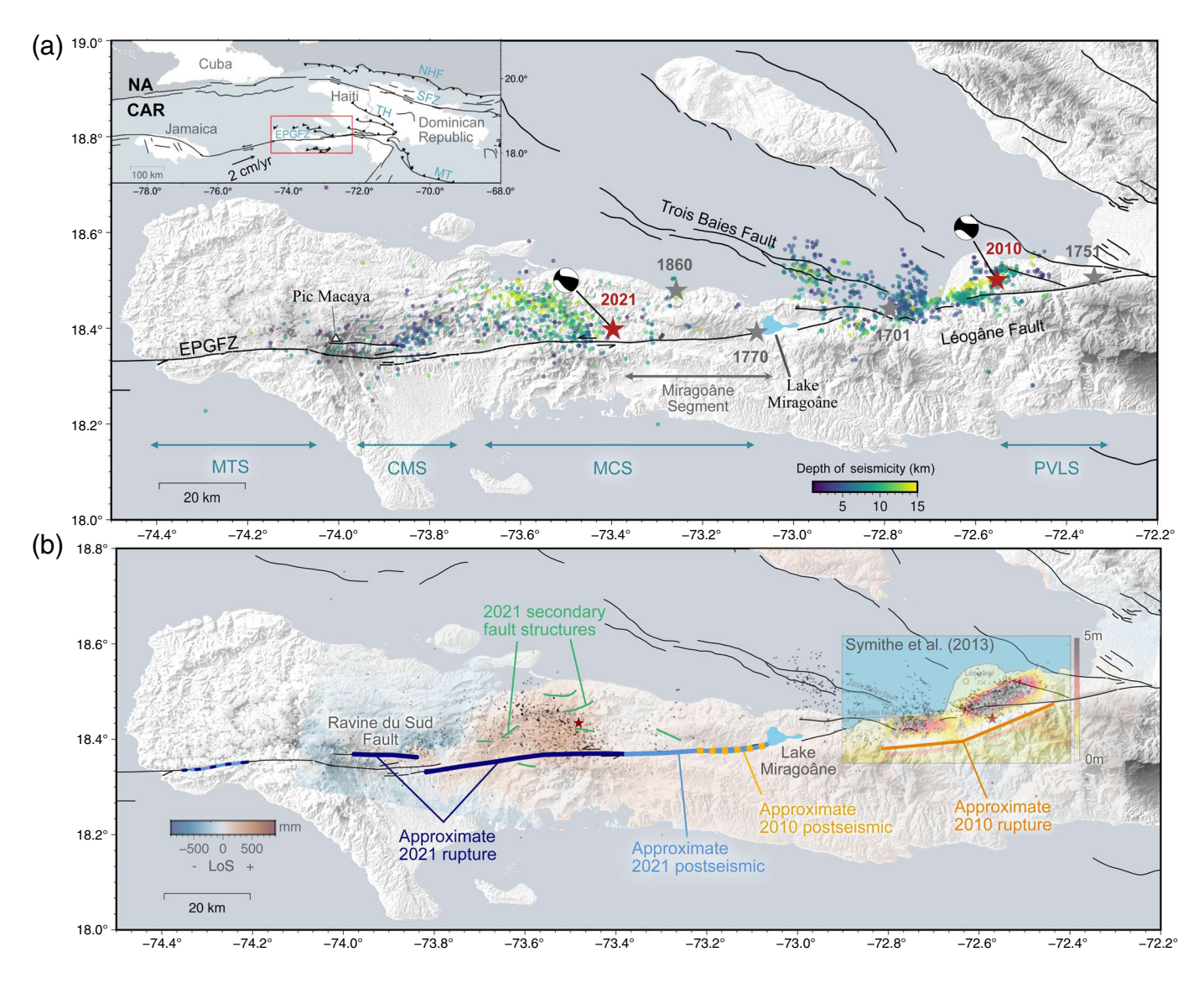


Figure 1. (a) Overview of the southern peninsula of Haiti, highlighting major geographic markers, fault zone locations, and historic earthquakes. Major historic earthquakes are marked by stars, with red stars highlighting the locations of the 2021 $M_{\rm w}$ 7.2 and 2010 $M_{\rm w}$ 7.0 epicenters with Centroid Moment Tensor (CMT) solutions. Aftershock locations are shown with circles colored by event depths. Aftershock locations following the 2010 event on the Léogane blind-thrust fault and Trois Baies fault are from Douilly *et al.* (2013). Aftershock locations following the 2021 event are from the Ayiti-Séismes network (Calais *et al.*, 2022). Mapped Enriquillo—Plantain Garden fault zone (EPGFZ) faults (black lines) are from Saint Fleur *et al.* (2020). The previously understood segmentation of the Enriquillo—Plantain Garden fault zone from Saint Fleur *et al.* (2020) is shown with horizontal blue arrows, and designates the Macaya—Tiburon segment (MTS), Clonard—Macaya segment (CMS), Miragoâne—Clonard segment (MCS), and Pietonville—Léogane segment (PVLS). The unruptured segment of the MCS is labeled as

the Miragoâne segment. The upper left side panel shows an overview of the regional teconic setting where the following abbreviations are used: EPGFZ, Enriquillo—Plantain Garden fault zone; MT, Muertos trough; NHF, North Hispaniola fault; SFZ, Septentrional fault zone; and THB, Transhaitian belt. (b) Summary of faults active in the 2010 and 2021 ruptures. The approximate extents of the 2021 and 2010 coseismic and postseismic slip features are shown with colored lines. Note that the north-dipping Leogane blind-thrust fault is on the north side of the mapped Enriquillo—Plantain Garden fault (EPGF) that ruptured in 2010 Symithe *et al.* (2013) but has a surface projection that appears on the south side of the EPGF (solid orange lines). The line-of-sight (LoS) deformation from the descending Advanced Land Observation Satellite (ALOS)-2 track D138 coseismic pair (10 December 2019—17 August 2021) is overlaid for context where the region of red indicates uplift. The color version of this figure is available only in the electronic edition.

The current maps estimate the seismic hazard from the major crustal faults including the strike-slip Enriquillo-Plantain Garden fault in the south and Septentrional fault in the north, and the Transhaitian belt (THB)—a series of en enchelon fold

and thrust faults north of Port-au-Prince. The maps include the contributions from the north Hispaniola fault subduction boundary and the Muertos trough subduction zone to the south (Fig. 1). The EPGFZ was considered to be a single segment from the western limit of the 2010 rupture to the western coast of Haiti. Considering observations of the 2010 and 2021 earthquakes together can provide insight on rupture segmentation and could, therefore, play an important role in further refining the distribution of seismic hazard within the fault zone.

The 12 January 2010, earthquake occurred within the EPGFZ on the previously unmapped Léogâne blind-thrust fault (Calais et al., 2010; Mercier de Lepinay et al., 2011), with upward motion on the eastern part of the rupture in a direction opposite to that indicated by the regional topography (Hayes et al., 2010; Hashimoto et al., 2011). This upward motion resulted in up to 0.64 m of coastal uplift (Hayes et al., 2010) and 0.40 m of broad subsidence in the coastal mountain range (Hashimoto et al., 2011). A significant amount of triggered seismicity followed the mainshock on the adjacent offshore Trois Baies thrust fault (Douilly et al., 2013; Fig. 1). Coseismic static and kinematic slip models of the 2010 earthquake showed that the rupture propagated westward with two main slip patches—one with a major component of dip-slip in the east and another primarily with strike slip in the west (Calais et al., 2010; Meng et al., 2012; Symithe et al., 2013). Calculations of the change in Coulomb failure stress (dCFS) from the coseismic slip showed a region of estimated stress increase collocated with aftershock observations to the west of the 2010 rupture on the Trois Baies fault and on the EPGF at depth. This suggested the possibility of higher hazard in these regions (Symithe et al., 2013). Calculations of the cumulative stress changes from major historical events showed loading on adjacent fault segments over the course of several earthquake cycles (Ali et al., 2008). Dynamic rupture modeling experiments for the 2010 earthquake explored the conditions that could explain the pattern of rupture on the Léogane fault, without rupture of the main EPGF, nor the Trois Baies fault (Douilly et al., 2015). It was found that variations in frictional properties were necessary for rupture to propagate from the eastern to western plane of the Léogane fault. However, the models suggest that the rupture did not jump to the Trois Baies and Enriquillo faults due to their orientations with respect to the Léogane fault. The interpretation of the EPGFZ as a single, segmented strike-slip fault may, therefore, be oversimplified.

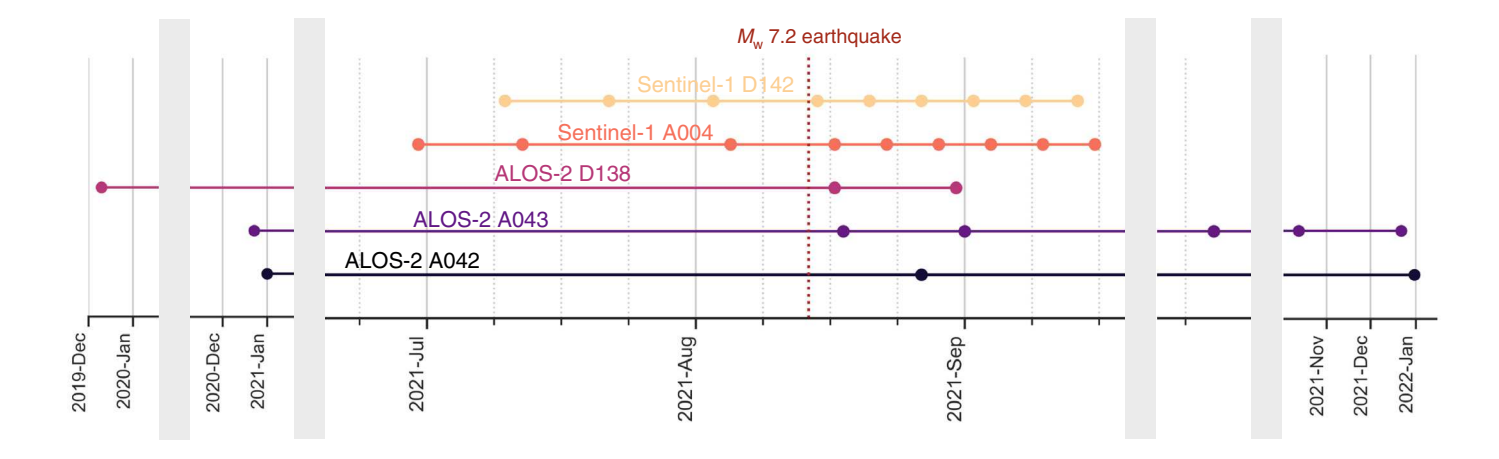
The 14 August 2021 $M_{\rm w}$ 7.2 earthquake did not rupture the segment identified with the highest dCFS following the 2010 event. Instead, it ruptured from the center of the Miragoâne–Clonard segment (MCS) and continued approximately 80 km westward (Fig. 1). Aftershock locations for the 2021 $M_{\rm w}$ 7.2 event were calculated by the local network, Ayiti-Séismes, which includes the new RaspberryShake sensors that were deployed in local homes in a citizen science initiative (Calais *et al.*, 2022). The seismicity on the north side of the surface trace indicates that the fault is likely north dipping, although there are not yet clear planar features identified in

the aftershock locations. Okuwaki and Fan (2022) identified two distinct rupture episodes associated with this event, first rupturing a blind-thrust fault in the east before jumping to a strike-slip fault westward. The aftershock distribution and backprojection models both show that the two distinct ruptures were not contiguous (Calais et al., 2022; Okuwaki and Fan, 2022). Interferometric Synthetic Aperture Radar (InSAR) data are consistent with a rupture dominated by left-lateral strike-slip motion in the west and with dip-slip motion in the east (Calais et al., 2022; Maurer et al., 2022). The rupture pattern of the 2021 event closely resembles that of the 2010 earthquake and suggests that the accommodation of compression along this boundary may play a major role in strain partitioning. Neither the 2010 nor the 2021 earthquake ruptured the intervening Miragoâne segment between the two event rupture planes, raising the question of whether this segment is seismically loaded or if it is accommodating strain in some other way. Observations of this complex rupture sequence are, therefore, highly relevant for both improving our understanding of seismic hazard in Haiti and in transpressive strike-slip margins, in general.

DATA

Two InSAR satellite missions were operational at the time of the 2021 event: Sentinel-1 twin satellites operated by the European Space Agency (ESA) and ALOS-2 operated by the Japanese Aerospace Exploration Agency. Both InSAR data sets are used to generate interferograms and derived products for this study. InSAR interferograms are formed using the difference in radar return phase between two satellite passes, with fringes representing small, coherent deformation of the Earth's surface in the line-of-sight (LoS) of the radar. After unwrapping, these interferograms provide a broad view of surface deformation between two Synthetic Aperture Radar acquisitions. Ascending and descending passes provide two unique look angles over the region that constrains the total deformation. The east-west trend of the EPGF and roughly east-west look angles of ascending and descending InSAR satellite passes for both the missions in this region align fortuitously, making InSAR observations especially sensitive to fault-parallel motion, which is of the greatest interest. These two InSAR missions have complementary strengths and limitations. In particular, we are concerned with radar wavelength, acquisition mode, and repeat acquisition times.

The longer ALOS-2 wavelength (L-band, 22.9 cm wavelength) makes it more resistant to decorrelation due to vegetation than the shorter Sentinel-1 wavelength (C-band, 5.5 cm wavelength), which is a major concern in tropical Haiti. Each satellite instrument can operate in a variety of acquisition modes, each with a corresponding swath footprint and resolution. The ALOS-2 repeat descending passes that cover this event are in the lower resolution ScanSAR mode (350 \times 350 km swaths, with roughly 100 m resolution), whereas the repeat



ALOS-2 ascending passes are in the higher resolution strip map mode (30 \times 30 km swaths, with roughly 4 \times 8 m resolution). Sentinel-1 acquisitions used in this study are in Interferometric Wideswath mode (250 km wide swaths, with 3×22 m resolution). ALOS-2 routine acquisitions are infrequent over Haiti, with the closest ALOS-2 repeat passes occurring more than six months prior to the earthquake for ascending passes and more than a year prior to the earthquake for descending passes (Fig. 2). Sentinel-1 acquisitions in this region are generally frequent and regular, with repeat times of 6-12 days. This short temporal baseline in Sentinel-1 data relative to ALOS-2 data would generally reduce phase decorrelation due to changes in the land surface properties between acquisitions. However, in this case there is a trade-off between the increased susceptibility to vegetation of Sentinel-1 data and its more frequent acquisitions. When combined, Sentinel-1 and ALOS-2 data have the capability to illuminate small, rapidly changing signals like postseismic slip, while also capturing a high-resolution deformation field and mitigating interference from vegetation.

METHODS

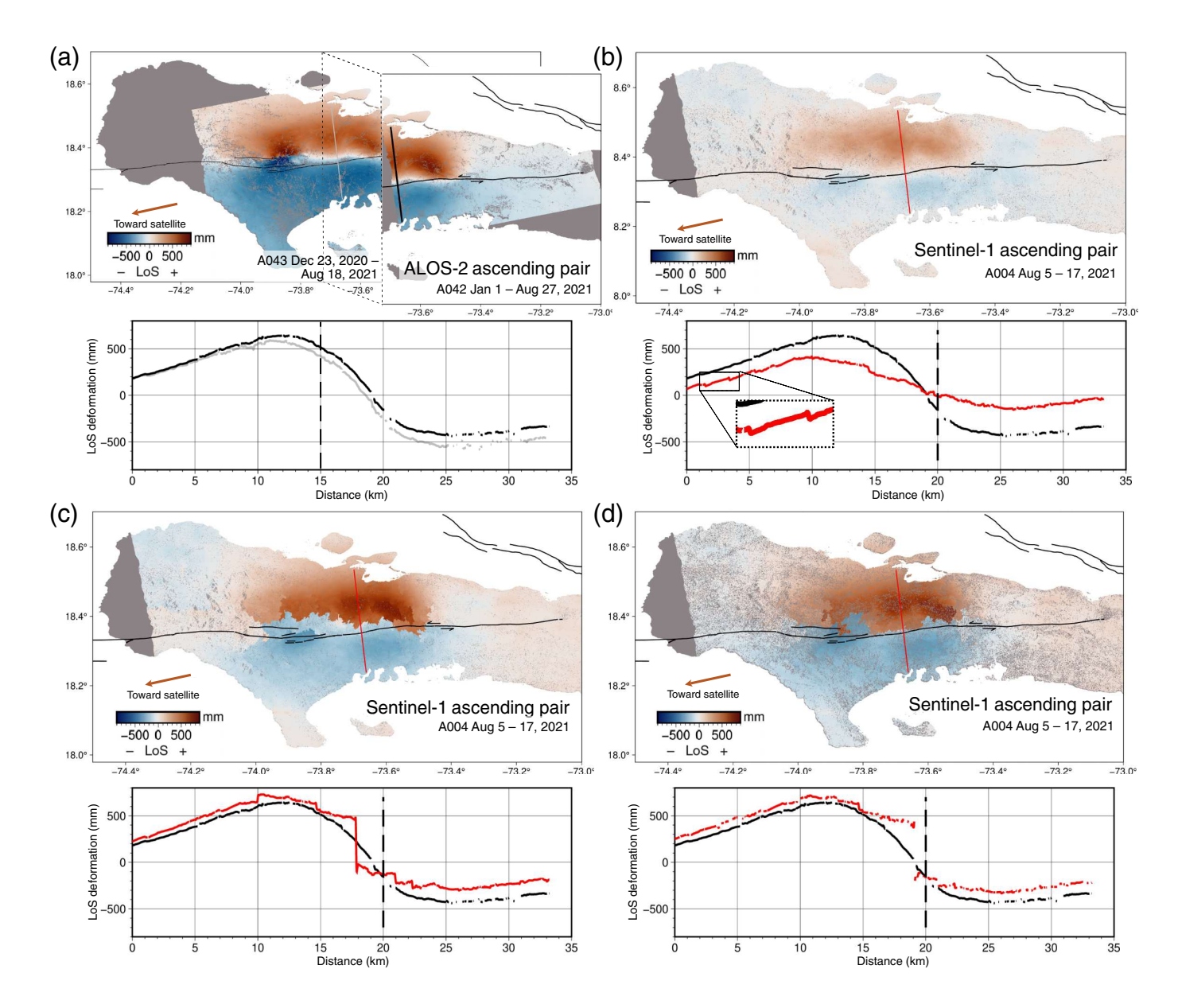
We compile Sentinel-1 and ALOS-2 repeat acquisitions surrounding the time of the 2021 earthquake, and use GMTSAR software to process the raw data (Sandwell et al., 2011; Wessel et al., 2013; Xu et al., 2017). Interferograms are Gaussian filtered at 200 m and resampled at 50 m before further processing. We unwrap the phase using the statistical cost, network flow algorithm for phase unwrapping (SNAPHU) (Chen and Zebker, 2002), with the nearest-neighbor interpolation over the low coherence areas and water surfaces (Shanker and Zebker, 2009). The resulting LoS plots (Fig. 3) show surface deformation in the LoS of the observing satellite, in which a positive LoS value indicates that the ground pixel has moved toward the satellite. Phase unwrapping is generally a nonunique process and requires parameter choices that affect the resulting LoS solution. These choices include phase filtering wavelength (applied prior to unwrapping), the minimum coherence threshold for pixels to be included in unwrapping, whether and how broadly to interpolate over low-coherence

Figure 2. Timeline of all Synthetic Aperture Radar (SAR) scene acquisitions used in this work with the vertical red dashed line marking the 14 August earthquake. Sentinel-1 acquisitions are frequent, with ascending and descending acquisitions less than two weeks before the 2021 earthquake. In contrast, ALOS-2 acquisitions are infrequent, with the closest usable ALOS-2 acquisitions prior to the earthquake more than 6 months before the earthquake. Note the breaks in the horizontal axis in gray, which represent large time periods between ALOS-2 acquisitions. The color version of this figure is available only in the electronic edition.

areas, and the maximum phase discontinuity that the unwrapping algorithm can assign. These parameters are calibrated by trial and error to minimize visually identifiable unwrapping errors in resulting LoS plots. The sensitivity of the unwrapping results to these parameter changes can be an indicator of the reliability of the data for unwrapping.

Phase unwrapping reliability

Phase unwrapping of ALOS-2 data from the 2021 event is more reliable than Sentinel-1 data due to its longer radar wavelength, enabling superior coherence. The region near the rupture in the Sentinel-1 coseismic interferograms could not be reliably unwrapped, likely due to extreme ground shaking near the fault and decorrelation due to vegetation. The unwrapping errors produced by Sentinel-1 coseismic pairs are illustrated in Figure 3, which shows a comparison between three unwrapping approaches used on the same Sentinel-1 ascending coseismic pair (Fig. 3b-d) versus the closest equivalent ALOS-2 ascending coseismic pair (Fig. 3a). Figure 3a shows two overlapping, ascending ALOS-2 coseismic pairs in stripmap mode: A043, spanning 23 December 2020-18 August 2021, and A042, spanning 1 January-22 August 2021. These pairs are unwrapped allowing a 15 phase cycle (1.72 m) discontinuity and interpolating regions with coherence below 0.1 over the nearest 300 pixels. The corresponding cross sections show a smooth deformation pattern that is continuous across the mapped EPGF and has the maximum change across the fault of around 700 mm in the LoS direction. Both the pairs cover the transect location, and the similarity in unwrapped LoS



solutions shown in the bottom panel of Figure 3a is an indicator that the unwrapping solutions are reliable. There are no clear signs of unwrapping errors, and the coherence is generally good, which supports the interpretation that this unwrapping solution is close to the true deformation field.

Figure 3b–d shows three unique unwrapping solutions for the closest equivalent Sentinel-1 ascending coseismic pair spanning 5–17 August 2021. Figure 3b shows the pair unwrapped allowing no discontinuity and interpolating regions with coherence poorer than 0.06 over the nearest 300 pixels. The corresponding cross section below shows a smoothed pattern of deformation with the maximum LoS deformation of about 400 mm, far below the ALOS-2 maximum deformation. This underestimation of maximum LoS deformation can be attributed to missed phase jumps, highlighted in the exploded view of Figure 3b. This illustrates that visual smoothness does not equate to a reliable unwrapping solution. Figure 3c shows the same pair with the same interpolation coherence threshold as

Figure 3. A comparison of ascending coseismic pairs unwrapped with different parameters. For each panel, the top inset shows the unwrapped LoS solution with a transect plotted perpendicular to the mapped EPGF (black). The bottom inset shows the corresponding LoS values along the transects plotted in gray, black, or red. The location of the main strand of the mapped EPGF (Saint Fleur *et al.*, 2020) is shown with the dashed vertical black lines in the cross sections. (a) Overlapping ascending ALOS-2 coseismic pairs in stripmap mode: A043, spanning 23 December 2020–18 August 2021 and A042, spanning 1 January–22 August 2021. (b–d) The Sentinel-1 ascending track A004 coseismic pair spanning 5–17 August, unwrapped using varying parameters. The ALOS-2 A042 LoS transect is shown in black in the panels (b–d) cross sections for comparison. The color version of this figure is available only in the electronic edition.

Figure 3b, but unwrapped allowing an 80 cycle (about 2.22 m) discontinuity. The corresponding transect has many more phase jumps due to the larger discontinuity allowance, with a maximum LoS deformation of about 750 mm, comparable to that of the ALOS-2 pair. This LoS plot contains phase unwrapping

errors seen as the irregular southern edge of the red region, which obscures the pattern of deformation near the mapped EPGF. Figure 3d shows the pair unwrapped allowing an 80 cycle (about 2.22 m) discontinuity and interpolating regions with coherence below 0.1 over all pixels. The corresponding transect shows a smoother pattern of deformation than Figure 3c, with the maximum LoS of about 750 mm, but with a large discontinuity near the mapped EPGF and some unwrapping errors persisting on the eastern and western portions of the main rupture.

The comparison among the LoS solutions using varying unwrapping criteria (Fig. 3) illustrates the limitations of Sentinel-1 data for deducing the amplitude of the broad coseismic deformation pattern of this earthquake, in which there is a trade-off between the amplitude of the LoS deformation, and thresholds for phase cycle discontinuities and coherence. Maurer et al. (2022) suggested that a possible explanation for the significantly higher amplitude of the ALOS-2 A043 coseismic deformation relative to Sentinel-1 was that there was a significant amount of aseismic slip after the Sentinel-1 descending acquisition on 15 August, but before the ALOS-2 A043 acquisition on 17 August. They argue that this could be explained by an additional postseismic moment release equivalent to an $M_{\rm w}$ 6.8. We find that although there is evidence of postseismic shallow slip after 15 August, there is a lack of a clear, broad deformation signal in subsequent Sentinel-1 pairs spanning 15-21 August (D142) and 17-23 August (A004), which we would expect to capture any significant postseismic moment release (Fig. S1, available in the supplemental material to this article). Calais et al. (2022) used InSAR data in their modeling and observed high uncertainty in the near-fault region of the closest earthquake-spanning Sentinel-1 LoS observations. They chose to mask those values (to around 10 km north of the EPGF). The variability of Sentinel-1 unwrapping results in our analysis is consistent with this approach, and this unwrapping uncertainty could explain the difference in deformation amplitude between Sentinel-1 and ALOS-2 coseismic pairs. Therefore, we assume that ALOS-2 unwrapping results are more reliable for understanding the true LoS deformation, so we use only ALOS-2 pairs for broad coseismic deformation pattern analysis and interpretations of surface rupture. We primarily use Sentinel-1 results to resolve postseismic creep on faults.

Phase gradient analysis

Phase unwrapping is a useful technique for estimating the broad surface deformation pattern in response to a rupture. However, the large amplitude broad deformation field may obscure small-scale deformation features with smaller amplitudes. In contrast, calculating the interferometric phase gradient directly from the unfiltered, full-resolution interferogram (Sandwell and Price, 1998) highlights sharp changes in radar phase, amplifying the appearance of small-scale deformation features. Given the expression for interferometric phase at location, x, in terms

of the real (R) and imaginary (I) components of the complex interferogram:

$$\phi(x) = \tan^{-1}\left(\frac{I}{R}\right),\tag{1}$$

we can then use the chain rule to derive an expression for the phase gradient in terms of *R* and *I*:

$$\nabla \phi(x) = \frac{R\nabla I - I\nabla R}{R^2 + I^2},\tag{2}$$

in which $\nabla = \frac{\partial}{\partial r}, \frac{\partial}{\partial a}$ and a is the azimuth (flight) direction, and r is the range (look) direction in radar coordinates (Sandwell and Price, 1998; Xu, Sandwell, Ward, *et al.*, 2020).

This approach avoids the need for phase unwrapping, and the solution can be stacked directly to enhance the signal-tonoise ratio. The ability to stack solutions is important because taking the gradient amplifies noise in the interferogram. We apply a square Gaussian filter with a large wavelength (200 m) to the phase gradient product to suppress noise. We take the gradient in both the azimuth (flight) and range (look) directions but find that the gradient in the azimuth direction tends to resolve features more clearly, likely because most active features are aligned more closely to the range direction than to the azimuth direction. Phase gradients calculated in the range direction are shown in Figure S2 and do not reveal any new features. The offset direction of phase gradient features cannot be interpreted directly from phase gradient plots. Instead, corresponding LoS images are used to guide the interpretation. Phase gradient features are largely unresolvable from Sentinel-1 interferograms, even after stacking a large number of interferograms (Fig. S3). This is likely due to the higher noise from phase decorrelation due to vegetation, which is then amplified by the phase gradient calculation. However, interferograms from ALOS-2 ascending tracks A043 and A042, which are in stripmap mode have excellent coherence and resolution, rendering clear linear features in the resulting phase gradient plots.

RESULTS

The complete set of InSAR products from Sentinel-1 and ALOS-2 were examined for evidence of slip surrounding the main rupture zone. This dataset is openly available for download (Yin *et al.*, 2022). We describe three categories of observed surface deformation features in the following section: (1) broad coseismic deformation pattern; (2) postseismic slip on the mapped EPGF adjacent to the main rupture; and (3) slip on secondary fault features off of the mapped EPGF.

Broad coseismic deformation

The broad coseismic deformation pattern of the 2021 earthquake is illuminated by earthquake-spanning interferograms from the ascending and descending ALOS-2 coseismic pairs shown in Figure 4. Figure 4a,b shows overlapping ascending

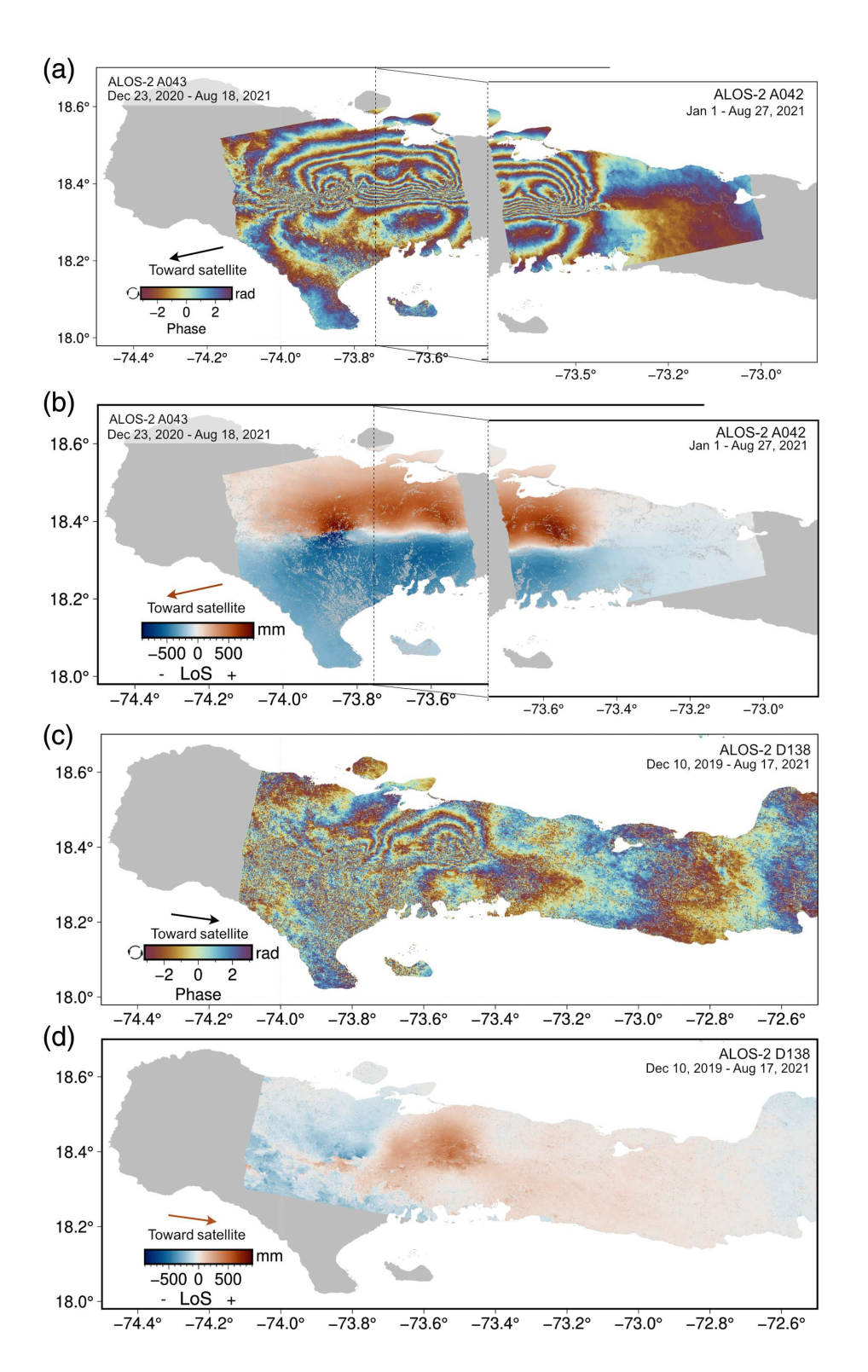
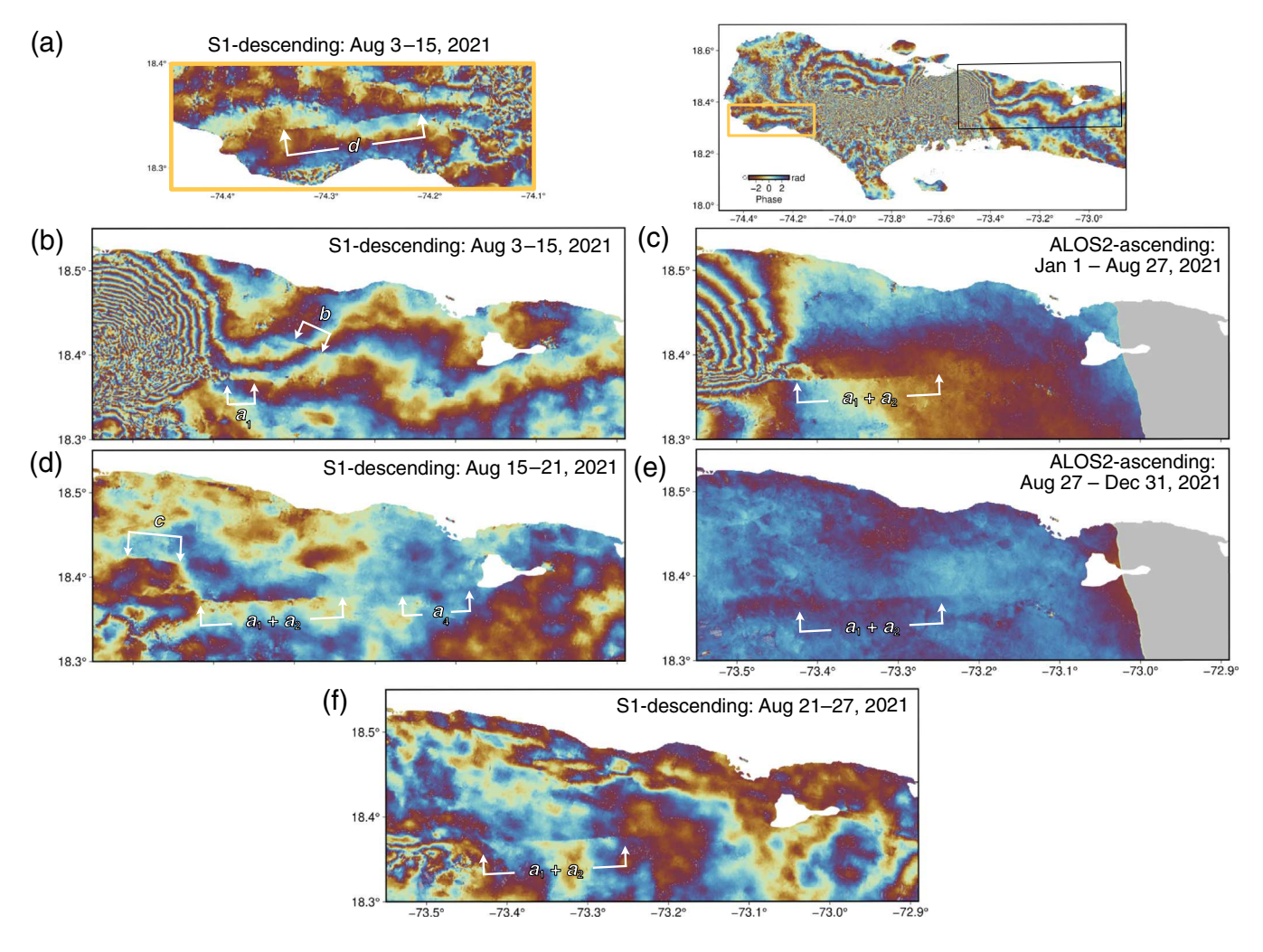


Figure 4. ALOS-2 ascending and descending coseismic pairs shown as wrapped phase and unwrapped LoS deformation. (a) ALOS-2 wrapped phase in stripmap mode from the coseismic pairs for ascending track A043 (left, 23 December 2020–18 August 2021) and ascending track A042 (right, 1 January–27 August 2021). (b) Unwrapped phase, converted to LoS deformation for A042 and A043 coseismic pairs. The red represents positive motion of the ground surface in the direction of the arrow and shows a deformation pattern dominated by left-lateral strike-slip motion. (c) ALOS-2 wrapped phase in ScanSAR mode from the coseismic pair (10 December 2019-18 August 2021) for descending track D138. (d) Unwrapped phase converted to LoS deformation for the D138 coseismic pair. The red lobe to the east indicates a region of significant uplift, whereas the western lobe of deformation continues to be dominated by left-lateral deformation. The color version of this figure is available only in the electronic edition.

ALOS-2 tracks A043 (left, 23 December 2020-18 August 2021) and A042 (right, 1 January-27 August 2021) acquired in stripmap mode spanning the earthquake. Figure 4a shows the wrapped phase with fringes converging near the mapped EPGF, indicating deformation caused by the main rupture. Figure 4b shows the unwrapped LoS deformation, with red indicating motion up and to the west extending from approximately 74° W to 73.4° W. Figure 4c,d shows the descending pair (track D138), acquired in ScanSAR mode, spanning 10 December 2019-18 August 2022, which are the closest acquisitions before and after the earthquake. LoS deformation in Figure 4d shows a region of red, indicating motion up and to the east confined to the eastern portion of the rupture, which is consistent with dip-slip motion. This observation agrees with the moment tensor solution for the event that shows strike-slip motion with a component of dip slip (U.S. Geological Survey [USGS], 2021), other finitefault rupture solutions (Calais et al., 2022; Maurer et al., 2022), and backprojection estimates (Okuwaki and Fan, 2022).

The coseismic LoS plots show a smooth transition from red to blue across the EPGF through most of the central and eastern rupture (from approximately -73.8° to -73.5°). This smooth transition indicates that the rupture likely did not reach the surface through this section. However, in the western portion of the rupture zone, there is a sharp transition from dark red to dark blue in both ascending and descending LoS



plots (from approximately -74.0° to -73.8°), suggesting surface rupture in this area. This surface rupture coincides with the mapped Ravine du Sud fault, indicating that this fault was active during the earthquake.

Postseismic slip on the EPGF

Postseismic slip on the order of ~2 cm occurred on the mapped EPGF to the east of the main rupture in the two weeks following the earthquake. The propagation of slip was captured by consecutive Sentinel-1 and ALOS-2 pairs, seen as offsets in the wrapped phase interferograms in Figure 5, in which offsets indicate surface deformation. We use a perceptually uniform and cyclic color palette (romaO) to plot wrapped phase to reduce bias in the identification of features (Crameri *et al.*, 2020). More confidence was given to features that appeared in both wrapped interferograms and phase gradient plots, that appeared in multiple interferogram pairs, and have more than ~7 mm of offset in the wrapped phase images.

Figure 5b shows Sentinel-1 descending track D142 3–15 August pair, which is dominated by the coseismic deformation signal from the mainshock, seen as concentric curved fringes. However, to the east of that coseismic deformation pattern, feature a_1 is identified with a length of approximately 5 km

Figure 5. Consecutive pairs of Sentinel-1 descending track D142 and ALOS-2 ascending track A042 wrapped phase. Truncated phase features are highlighted with white arrows and indicate possible postseismic deformation. An inset in the upper right hand corner outlines the regions shown in panels (a-f). (a) Sentinel-1 descending track D142 3–15 August pair zoomed to the orange outlined area to the west of the main rupture; feature *d* is identified extending west of the main rupture. (b) Sentinel-1 descending track D142 3–15 August pair zoomed to the black outlined area to the east of the main rupture. (c) ALOS-2 ascending track A042 1 January–27 August 2021 pair. (d) Sentinel-1 descending track D142 15–21 August pair. (e) ALOS-2 ascending track A042 27 August—31 December 2021 pair. (f) Sentinel-1 descending track D142 21–27 August pair. The color version of this figure is available only in the electronic edition.

where the fringes are offset. It is possible that this phase offset occurred as part of the coseismic rupture. However, another explanation is that postseismic slip occurred on a_1 in the day following the earthquake (i.e., before the second Sentinel-1 pass on 15 August). The latter interpretation is supported by evidence of continued slip on feature a in the following InSAR pairs. In addition to slip on the mapped EPGF, a secondary feature b is identified in this pair to the north of the EPGF, but no further slip is observed on this segment in subsequent pairs. Figure 5a identifies feature d in the same

coseismic pair (3–15 August 2021) but to the west of the main rupture on the mapped EPGF. Feature d has a length of approximately 8 km and does not appear in any subsequent pairs, so it could reasonably have occurred during the earthquake as coseismic slip, as is attributed by Maurer $et\ al.\ (2022)$, or in the day after the earthquake as postseismic slip. Because this feature is observed only in this coseismic pair, its extent and timing are less certain than that of feature a.

Figure 5d shows the Sentinel-1 descending track D142 15–21 August pair for the following time period, in which the feature identified in Figure 5b persists on a_1 and extends an extra \sim 10 km to the east, identified in the figure as feature $a_1 + a_2$. This is clearly interpretable as postseismic slip with an approximate maximum offset of 18 mm identified in the LoS direction across the fault. There appears to be a gap (unlabeled segment a_3) between slip on $a_1 + a_2$ and slip on feature a_4 that abuts Lake Miragoâne. In addition, we identify an \sim 5 km secondary fault feature c that shows postseismic slip also occurring off of the main fault, with an orientation similar to segment b. Figure 5f shows Sentinel-1 descending track D142 21–27 August pair, in which slip continues along $a_1 + a_2$ but is no longer visible on a_4 . No deformation is observed in the subsequent pairs of this Sentinel-1 descending track.

Figure 5c shows ALOS-2 ascending track A042 1 January–27 August pair, which covers the same time period as Figure 5b,d,f combined. The direction of phase offsets in both the ascending and descending images of feature *a* indicates that the motion on feature *a* is primarily left lateral in the direction of the prevailing tectonic motion. Cumulatively, feature *a* persists for roughly 50 km to the east of the main rupture and is active for approximately two weeks following the earthquake. For each of these identified features, the slip is likely constrained to a very shallow portion of the crust, because there is no broader deformation pattern associated with it.

Figure 5e shows ALOS-2 ascending track A042 pair spanning 27 August–31 December. This pair shows a small amount of offset on a_1+a_2 that accumulates after 27 August. However, no slip is observed in Sentinel-1 pairs after 27 August. Therefore, a possible interpretation is that the slip shown in Figure 5f accrued on 27 August, just after the ALOS-2 27 August acquisition. The 27 August ALOS-2 acquisition occurred before the 27 August Sentinel-1 acquisition, which is consistent with this interpretation.

Slip on secondary faults

Phase gradient plots highlight areas of discrete offsets in the phase, without the need for phase unwrapping. Linear features are identified by sharp changes from the background gray to bright or dark. Phase gradient features indicate high positive or negative gradient in areas of concentrated deformation or higher strain. Figure 6 shows stacked phase gradient values for ALOS-2 ascending track A042 and A043 pairs. This figure contains phase gradient results for all pair combinations between

23 December 2020 and 31 December 2021 (three pairs for A042 and five pairs for A043), calculated in the azimuth (flight) direction and then summed to amplify the magnitude of phase gradient values in features appearing in multiple images above the random background noise. Deformation from the main rupture appears as a diffuse bright area surrounding the trace of the fault, generally without abrupt changes, because the rupture did not reach the surface along most of the fault.

Five main features are identified based on the stacked phase gradient plot (Figure 6, labeled a–h). Feature a is identified east of the main rupture, confirming the wrapped phase analysis of postseismic slip on the EPGF, as discussed in the previous section. Features f and g are the clearest of the phase gradient features. They are identified as two separate features but could be viewed as a continuous feature that changes slowly from white (g) to black (f). Features e and h are identified less clearly than features f and g, and run subparallel to the EPGF. Other subparallel lines above and below these features could reasonably be identified as features in addition to e and e. However, we limit our discussion to the labeled features, which are the most visually apparent and appear in multiple products.

After features are identified in the stacked plot, further inspection of the individual pairs gives clues about when these features were active. Figure 7 shows coseismic (1 January-27 August 2021) and postseismic (27 August-31 December 2021) ascending ALOS-2 pairs, each with phase gradient calculated in the azimuth direction and a high-pass-filtered LoS deformation plot to interpret the sense of motion on these smaller features. Features f, g, h, and a are easily identified in the coseismic pair (Fig. 7a). However, features f, g, and a can also be identified in the postseismic time period (Fig. 7b), at least through 27 August 2021. In Figure 7b, we also identify an additional feature, *i*, which appears north of feature g, but with a similar curved shape. This feature is only identified in the 27 August-31 December 2021 pair, suggesting that this feature is only active in the postseismic period. High-pass filtered LoS plots (Fig. 7c,d) are used to interpret the sense of motion on each of these features. Figure 7c shows the northern side of the feature moving away from the satellite (relative to the southern side) on feature f but toward the satellite on feature g. Figure 7d shows the same sense of motion on features g and *a*, but the sense of motion is unclear on feature *f*. The motion on feature f is opposite to that on feature g, but the absolute sense of motion cannot be constrained from ascending pairs alone, and the phase gradient calculations for the corresponding descending ALOS-2 and Sentinel-1 pairs were not able to resolve these features due to poorer resolution and higher noise, respectively.

Slip following the 12 January 2010 earthquake

Postseismic slip was reported after the 12 January 2010 earthquake (Wdowinski and Hong, 2011). We reprocessed ALOS-1 data from 2010 to confirm this postseismic deformation and to determine its location relative to the 2021 postseismic slip. The wrapped phase from the ALOS-1 postseismic pair spanning 16

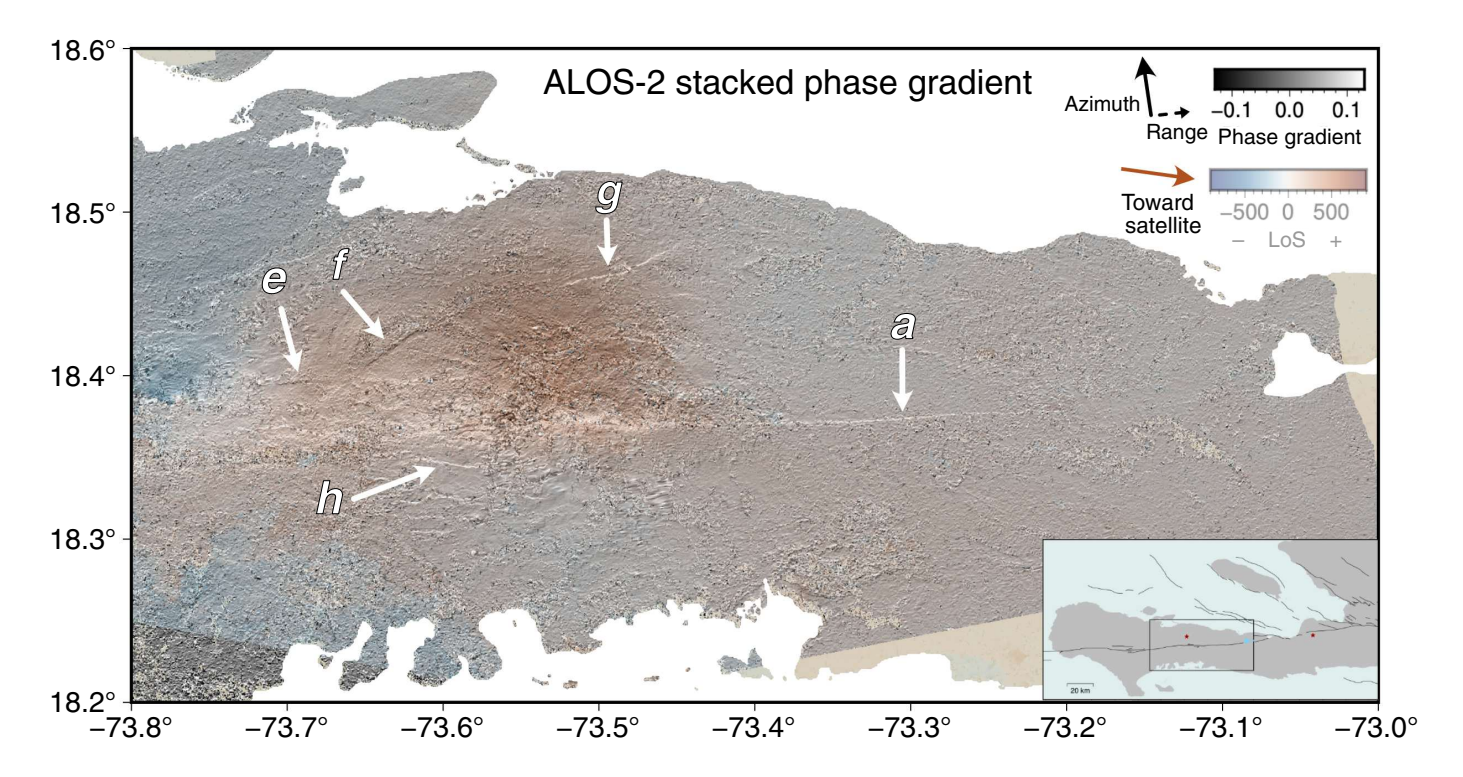


Figure 6. Stacked phase gradient of the interferometric phase taken in the azimuth (flight) direction. This stack sums the phase gradient from all ALOS-2 ascending track pairs between 23 December 2020 and 31 December 2021 (three pairs for A042 and five pairs for A043). The phase gradient is overlain with the LoS plot from ALOS-2 pair D138 for context.

The most apparent linear features are labeled a and e—h. Feature a is also observed as left-lateral slip in wrapped phase interferograms (Fig. 5). An inset in the lower right hand corner outlines the region shown in the context of the Southern Peninsula. The color version of this figure is available only in the electronic edition.

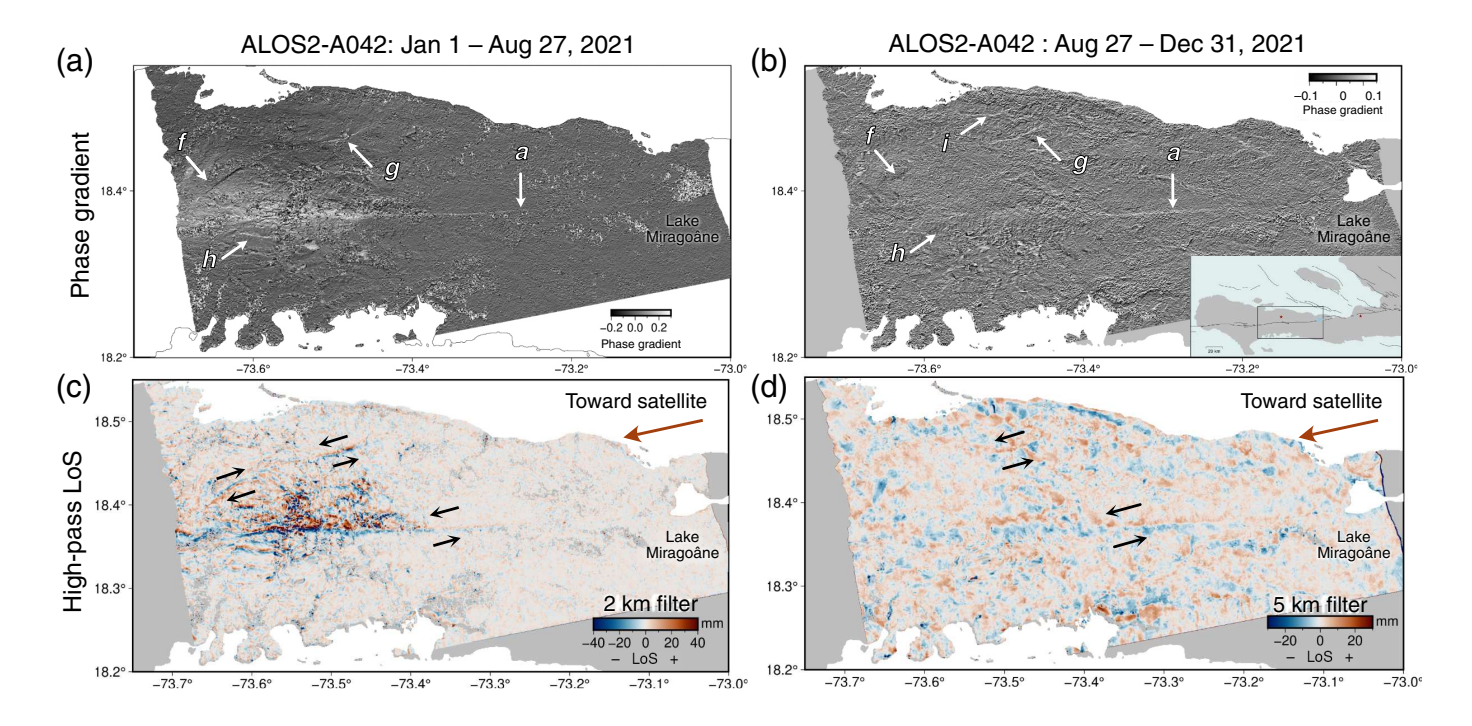


Figure 7. ALOS-2 ascending track 042 coseismic (left, 1 January–27 August 2021) and postseismic (right, 27 August–31 December 2021) pairs. (a,b) Each pair is shown as phase gradient calculated in the azimuth direction and (c,d) high-pass-filtered LoS deformation to highlight the sense of motion on these smaller features. Features are labeled in white, and the corresponding sense of motion on these features, if detectable, is indicated with black arrows on the LoS plots, below. (c) High-pass filtered with a 2 km Gaussian filter and

50 • Bulletin of the Seismological Society of America

shows the northern side of the feature moving away from the satellite (relative to the southern side) on feature f and toward the satellite on feature g. (d) High-pass filtered with a 5 km Gaussian filter and shows the same sense of motion on features g and a, but sense of motion is unclear on feature f. An inset in the lower right hand corner outlines the region shown in the context of the Southern Peninsula. The color version of this figure is available only in the electronic edition.

www.bssaonline.org Volume 113 Number 1 XXXX XXXX

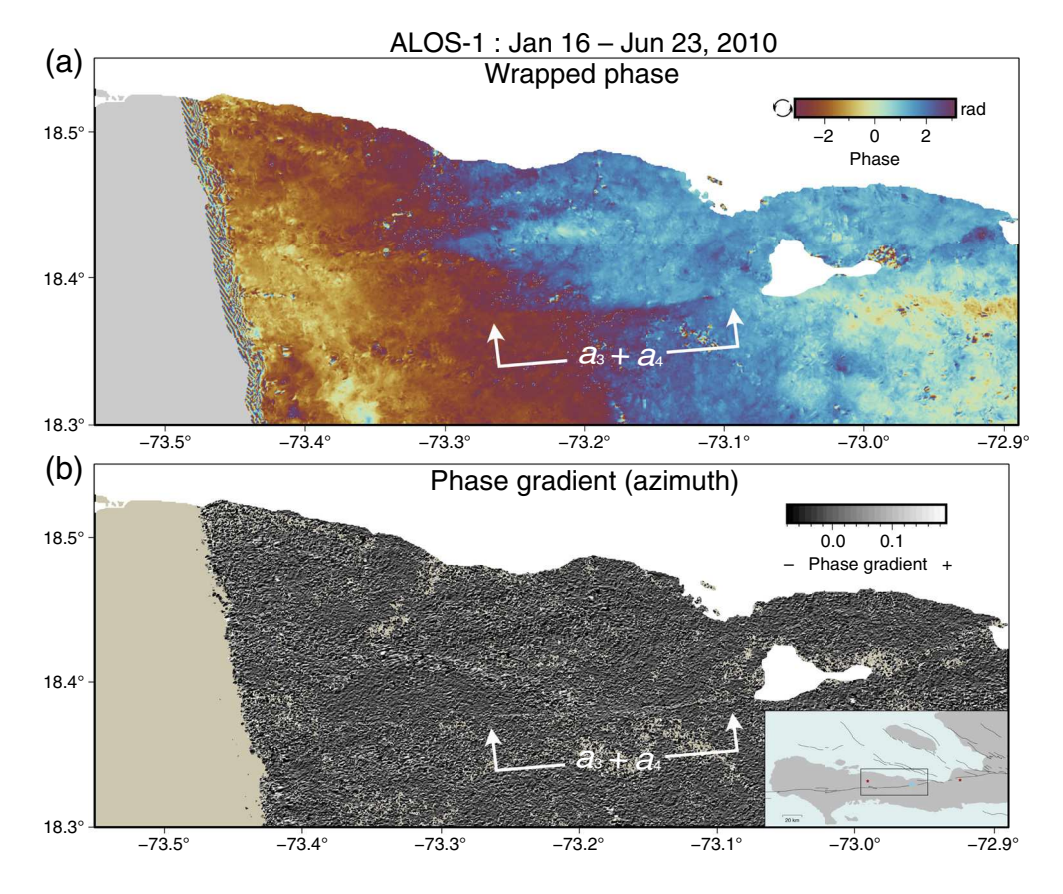


Figure 8. Postseismic deformation following the 2010 earthquake using ALOS-1 Interferometric Synthetic Aperture Radar (InSAR) pair spanning 16 January—3 June 2010. (a) Wrapped phase filtered at 200 m, postseismic offset indicated by black arrows. (b) phase gradient in the azimuth direction, postseismic offset indicated by white arrows. An inset in the lower right hand corner outlines the region shown in the context of the Southern Peninsula. The color version of this figure is available only in the electronic edition.

January-3 June 2010 shows a pattern of postseismic deformation on the mapped EPGF directly west of Lake Miragoâne. The phase gradient calculation in the azimuth direction illuminates linear feature a, indicating concentrated strain on the same feature in which postseismic slip is observed following the 2021 earthquake (Fig. 8). Although slip is not identified on the a_3 segment following the 2021 event, slip is detected on the a_3 segment following the 2010 event on a segment totaling ~17 km. The 2010 postseismic deformation was observed between 16 January 2010 (4 days after the earthquake) and 3 June 2010. The timing of this slip cannot be further constrained within this period. No postseismic deformation is observed in the subsequent ALOS-1 pair (3 June-19 July 2010). Similar to the postseismic deformation following the 2021 earthquake, the 2010 postseismic deformation on the EPGF decays within 1-2 km of the fault, suggesting that this slip is also very shallow.

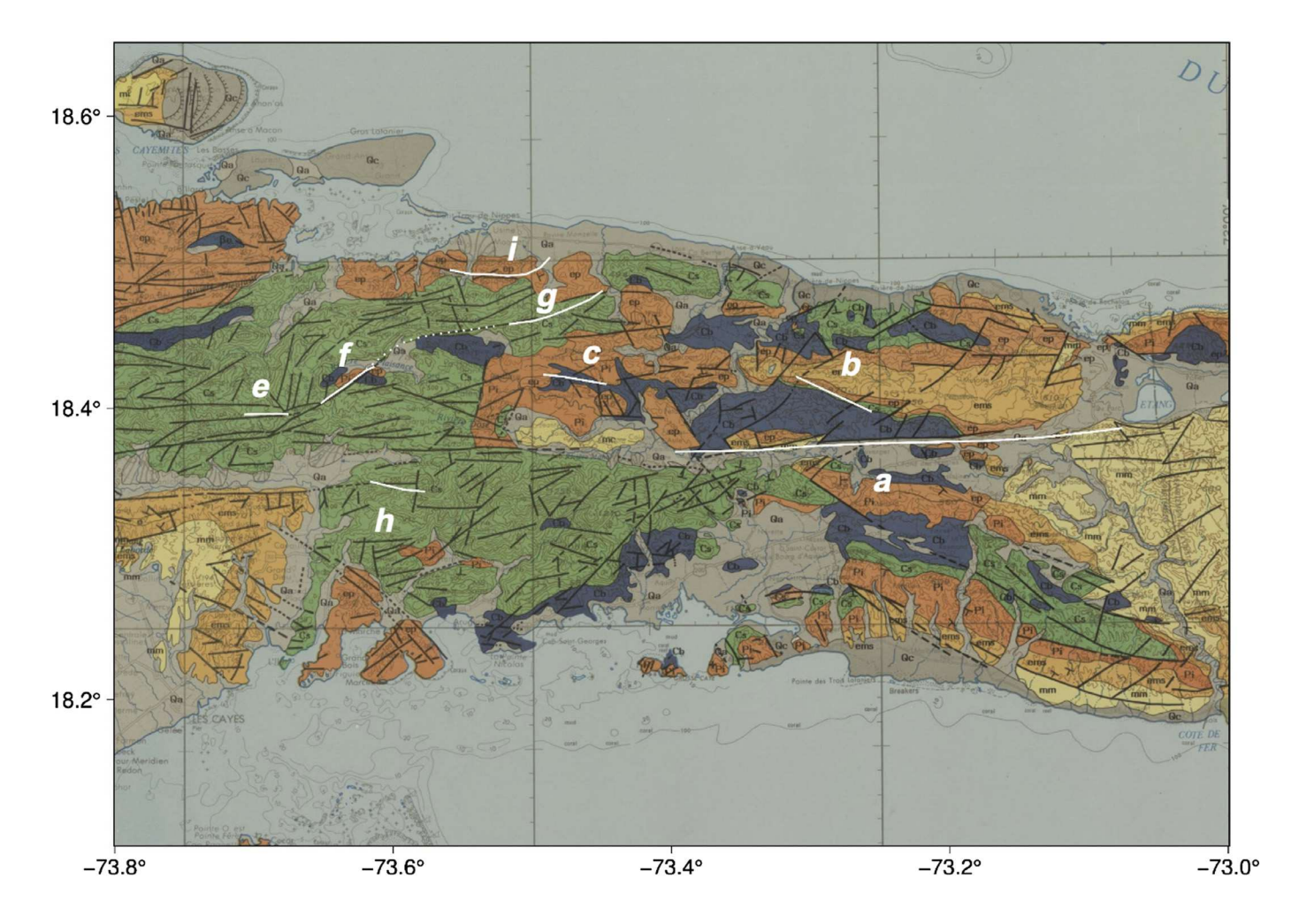
DISCUSSION

Taken together, InSAR observations surrounding the 2021 earthquake expose the evolution of deformation in the broader

EPGFZ during and after the event. Observations of the broad coseismic deformation field are consistent with two broad zones of deformation: one to the west with pure left-lateral strike-slip motion and one to the east with a significant component of dipslip motion. The maximum LoS deformation is ~ 1 m. We find strong evidence for surface rupture with offsets of ~1.5 m in the LoS direction on the western portion of the segment on the mapped Ravine du Sud fault. Wrapped phase and phase gradient analysis shows postseismic left-lateral offsets on the order of ~2 cm in the LoS direction on the mapped EPGF to the east of the main rupture. This feature is active for ~2 weeks following the mainshock. There is evidence for similar postseismic deformation on this same segment of the EPGF following the 2010 earthquake, occurring at least four days after the earthquake, although the timing of this slip is less well constrained. Finally, there is an extensive evidence for the involvement of

secondary fault features that were active during the coseismic period and the two-week period following the earthquake. Slip direction on these secondary faults is not well constrained and is likely limited to the shallow crust. The offsets on these secondary fault features are much smaller than the coseismic offsets, so these features are likely more useful as indicators of surface response than as significant contributors to strain rate for moment release.

To better understand the origin of the secondary fault features, we compare features a-i to a published geologic map Bien-Aime-Momplaisir et al. (1988) identifying faults in the southern peninsula of Haiti (Fig. 9). In the southern peninsula, massive Cretaceous oceanic basalts of the Caribbean Large Igneous Province Dumisseau Fm (Cenomanian to Santonian in age, 95–83 Ma, shown in slate grey) have been uplifted and exposed at the core of folds that formed in response to compressional tectonic motion (Mann et al., 2002; Calais et al., 2016). These exposed basalts are surrounded by younger overlying sedimentary units, namely the Cretaceous pelagic limestones of the Macaya Fm (Campanian–Maastrichtian in age, 80–66 Ma, shown in



green), and the still younger sedimentary units of the *Rivière Glace Fm* (Paleocene and Lower Eocene in age, 65–60 Ma, shown in orange; Mann *et al.*, 1995).

In Figure 9, feature a corresponds to the well-documented expression of the main fault strand of the EPGF. Features c and h do not coincide clearly with mapped faults. Feature b occurs at approximately the boundary between outcrops of the oceanic basalts (slate grey) and younger sedimentary units (orange). Feature e is coincident with a mapped fault in the pelagic limestones (green). Finally, features f and g both coincide well with mapped faults. The phase gradient images give some indication that the fault illuminated at f and g is continuous beneath the Quaternary alluvium that separates the fault traces on the geologic map, at the northern limit of where the Cretaceous basalts are exposed at the surface.

The younger sedimentary units (in orange, light green) are generally less competent than the more solid, uplifted oceanic basalts. We suggest that faults may be more difficult to identify in the field within or at the contact between the sedimentary units and the basalts. In addition, the boundary between stronger basalts and weaker sedimentary units might be a localized zone of weakness where faults could preferentially occur (for example, feature *b*). There are other more subtle features on the phase gradient map that may be interpreted as

Figure 9. Geologic fault map of Haiti originally published by (Bien-Aime-Momplaisir *et al.*, 1988) overlaid with features from the 2021 earth-quake identified from InSAR data (white). Massive Cretaceous oceanic basalts of the Caribbean Large Igneous Province (CLIP), Cenomanian to Santonian in age (95–83 Ma), shown in slate grey. Upper Cretaceous pelagic limestones of the *Macaya Fm* (Campanian–Maastrichtian in age, 80–66 Ma) shown in green. Younger Paleocene and Lower Eocene sedimentary units of the *Rivière Glace Fm* (65–60 Ma), shown in orange (Bien-Aime-Momplaisir *et al.*, 1988). The color version of this figure is available only in the electronic edition.

faults. However, we limit this discussion to features a–i, in which we have the most confidence based on their clarity and persistence in multiple images. The agreement between some features identified in InSAR data with previously mapped faults suggests that these faults were reactivated in the 2021 earthquake. One possible interpretation of the reactivation of these faults is that the uplift observed as dip-slip motion on the eastern portion of the fault rupture is accompanied by compressional motion on a blind-thrust fault at depth. Global Positioning System (GPS) observations on the southern peninsula indicate a combination of lateral strike slip at a rate of \sim 5 mm/yr and reverse slip of \sim 2 mm/yr (Calais *et al.*, 2010), which could be producing something akin to the flower

structures interpreted in other areas of the EPGFZ (Mercier de Lepinay *et al.*, 2011; Saint Fleur *et al.*, 2015).

To better understand the significance of the surface deformations observed surrounding the 2021 Haiti earthquake, it is useful to compare and contrast the observed slip behavior occurring (1) on the main EPGF and (2) on secondary faults associated with the Haiti earthquake to observations of similar slip behavior associated with other earthquakes:

Postseismic slip on the main fault

We observe postseismic slip on the main EPGF adjacent to the fault rupture unfolding for two weeks following the Haiti earthquake. This type of feature was investigated in a similar environment for the 1999 Izmit and Ducze earthquakes on the north Anatolian fault, in which InSAR analysis showed postseismic slip on the main fault from three to ten years after the earthquake, within the limits of the mainshock rupture zones (Hussain et al., 2016). However, the InSAR observations were not able to capture the early spatial distribution of slip. Instead, they were used to solve for along-fault variations of steady state creep. The early evolution was investigated using GPS observations from two near-fault sites to describe the period of early postseismic slip. The observations from Haiti highlight the usefulness of InSAR to identify the individual periods of slip with the higher temporal resolution of the weekly Sentinel-1 imagery and show that there is variation of early slip along the fault in space as well as in time.

InSAR, GPS, and creepmeter observations of the 2004 Parkfield earthquake on the San Andreas fault found postseismic slip occurring for ~7 days following the mainshock. The crossfault offset was ~10 cm, larger than that observed following the 2021 Haiti event (Jiang et al., 2021). Parkfield results indicated that shallow slip migrated from above the main slip patch and spread to the north and the south of the main rupture in the 24 hr after the earthquake and persisted for at least 7 days. The postseismic slip on the main fault contributed nearly the equivalent moment as was released in the mainshock. InSAR imagery and GPS data were combined to determine the total postseismic slip over the 3 months following the earthquake. However, InSAR data alone did not provide sufficient time resolution to break down the spatial distribution of slip further (Johanson, 2006; Langbein, 2006). In Haiti, shallow slip extended beyond the rupture in the first 24 hr, as occurred in Parkfield, but with much smaller amplitude. A denser sampling in time for Haiti compared to Parkfield provided subsequent images to show that the spatial distribution of slip accruing on adjacent sections of the main fault migrated over the 7-14-day time period, whereas this information was not accessible for Parkfield.

Following the 2014 Kangding, China, earthquake, Sentinel-1 InSAR observations were used to construct an average LoS displacement rate over 1800 days (Li and Burgmann, 2021). They solved for shallow creep from short wavelength filtered InSAR time series near the fault after removing a deep

slip component. The shallow steady-state creep rate varied along strike from 0 to ~ 10 mm/yr along the fault. They were also successful in distinguishing different decay rates of postseismic creep for different segments along the fault with InSAR.

These examples illustrate that postseismic creep is often observed with InSAR on strike-slip faults following a major earthquake. These observations have often been used to estimate variations in creep rate that indicate varying frictional behavior along the length of the faults. InSAR data from Haiti shows that phase gradient maps can be used to observe the spatial distribution of early slip. This suggests that past earthquakes could be revisited to further investigate the details of the spatiotemporal variation in slip and, in particular, extend the investigation farther away from the main rupture segment to include the possibility of secondary fault structure activity. Characterizing the spatial distribution of creeping segments of strike-slip faults and the degree of fault coupling contributes to understanding the ground motion and hazards associated with potential ruptures on faults with different properties (Aagaard et al., 2013; Li and Burgmann, 2021).

The lack of recent rupture on the Miragoane segment of the EPGF raises questions about its seismogenic potential—a question complicated by InSAR observations of shallow postseismic slip. Although an analysis of seismic hazard on this segment is beyond the scope of this study, we can make a rough estimate of the accumulated seismic moment deficit by making some simplifying assumptions. We assume that the last major earthquake that could have occurred on this segment was in 1770 (McCann, 2006), and that the length of the unruptured Miragoâne segment is 36 km as shown in Figure 1a. This geometry assumes that the 2010 earthquake released moment on the EPGFZ east of Lake Miragoâne, even though that earthquake occurred on the dipping Léogane fault and not the main EPGF. If we assume an interseismic slip rate of ~9 mm/yr at depth (Symithe et al., 2015) on a vertical strike-slip EPGF over the last 252 yr (1770-2022) with the fault locked to a depth of 15 km (Frankel et al., 2011; Symithe et al., 2015) and a shear modulus of 45 GPa (Hayes et al., 2010), then the accumulated seismic moment is 5.51×10^{19} N·m. If this moment were to be released in a single seismic event, we estimate an available moment magnitude of $M_{\rm w}$ 7.1. We can also consider the impact that shallow slip could have in reducing this estimate. The postseismic deformation signals observed following both the 2010 and 2021 Haiti earthquakes decay rapidly with distance perpendicular to the fault (i.e., within about 1-2 km of the EPGF), consistent with subsurface slip that is confined to the shallow crust but locked beneath. Relatively short duration transient postseismic slip likely does not make a significant contribution to reducing the accumulated moment on this unruptured segment of the fault. If, however, the Miragoane segment were consistently slipping from the surface to 5 km depth, the moment deficit would be reduced to 3.67×10^{19} N·m, which could still produce an

event of $M_{\rm w}$ 7.0. This estimate would need to be revised after a longer time period to provide a better constraint on the amount of steady creep that was releasing moment aseismically and providing a potential reduction in seismic hazard. It can be considered an estimate of upper bound on the moment deficit.

Slip on secondary faults

A second major conclusion from this work is that secondary fault structures were active in the near field of the Haiti earthquake, that some of these structures were previously mapped faults, and that motion on these faults persisted for more than 2 weeks following the event. Earthquakes in the well-studied southern California region provide several analogous examples of slip on secondary faults in response to earthquake ruptures. InSAR observations of the 1992 Landers earthquake (Price and Sandwell, 1998) illuminated preexisting mapped faults within 50 km of the main rupture using phase gradient techniques. Because of the sparse InSAR repeat acquisitions at this time, the temporal evolution of this signal is uncertain. Similarly, Sandwell et al. (2000) used InSAR data to study the 1999 $M_{\rm w}$ 7.1 Hector Mine earthquake. Here, the phase gradient technique revealed triggered slip on adjacent faults within 4 days of the earthquake. Most recently, InSAR phase gradient techniques were used following the 2019 Ridgecrest earthquake (Xu, Sandwell, and Smith-Konter, 2020; Xu, Sandwell, Ward, et al., 2020) to reveal slip on hundreds of secondary faults. However, none of these examples provide documented observations of slip on secondary faults that persists for weeks, as we observe following the 2021 Haiti earthquake for feature f-g north of the main EPGF.

We consider separately examples of shallow creep observed with InSAR that were triggered by regional or distant earth-quakes, as opposed to earthquakes on the same fault system. (Bodin et al., 1994) showed creep on the southern San Andreas fault triggered by the 1992 Landers, Big Bear, and Joshua Tree earthquakes using creepmeter observations. The spatial extent of triggered slip on the southern San Andreas was captured by InSAR following the 2017 Chiapas earthquake (Tymofyeyeva et al., 2019), where creepmeters indicated that the timing corresponded to the passage of seismic waves. Surface slip was also triggered on the San Andreas fault by the 2010 El Mayor–Cucapah earthquake (Wei et al., 2011).

These studies taken together illustrate the challenge of distinguishing slip triggered by dynamic stresses due to the passage of seismic waves from slip triggered by changes in the static stress field. Additional observations such as creepmeters or continuous GPS are required to pin down the timing of the slip. In Haiti, the continuation of slip on secondary faults for at least two weeks after the earthquake makes it likely that the cause could not have been solely dynamic triggering. Further study of the mechanism for secondary fault reactivation could include exploration of major aftershocks or distant events during the later time period. A teleseismic event in Chile

was shown to trigger an increase in seismic tremor on faults in Haiti and presented some evidence of triggering an increase in aftershocks (Aiken *et al.*, 2016), so an extended study following the release of a final earthquake catalog could be useful.

Douilly *et al.* (2022) provides detailed cross sections of relocated aftershocks that define the north-dipping rupture plane beneath our mapped secondary features *f* and *g*. The scarcity of seismicity above 8 km suggests that our secondary features may represent surface response to motion or deformation in the block above the north-dipping fault. The sparse shallow seismicity may indicate antithetic faults above 8 km that are favorably oriented with respect to the stress change of the main shock. The relationship of the seismicity to our secondary faults should be further investigated.

CONCLUSIONS

The 2021 Haiti earthquake did not rupture the EPGFZ adjacent to the 2010 earthquake but skipped over the intervening Miragoâne segment. InSAR observations provide evidence of postseismic slip on this unruptured segment following both the earthquakes. Postseismic deformation following the 2021 earthquake accrued over approximately 40 km to the east of the rupture on the main strand of the EPGF. In some places, there was as much as 2 cm of cross-fault displacement. The slip signal persisted for approximately two weeks following the earthquake before decaying below the InSAR detection threshold. Deformation following the 2010 earthquake occurred on the same unruptured EPGF segment and extended from Lake Miragoâne to about 15 km to the west and occurred at least 4 days after the event. The amount of slip observed on this unruptured segment is not sufficient to compensate for the expected accumulated seismic moment in the gap, and therefore, the fault remains a significant hazard. In other strike-slip environments, especially in desert settings, using InSAR to determine the fault properties of creeping segments and the degree of coupling contributes to a better understanding of the hazard associated with potential future ruptures. This study illustrates the potential for this type of investigation in a tropical environment.

Secondary fault features revealed by phase gradient techniques indicate complex faulting to the north of the mapped EPGF. When cross referenced with existing geologic maps, these features take on new import as reactivated older fault features. This reactivation of secondary fault features agrees with the broad distribution of aftershock relocations north of the mapped EPGF (Calais *et al.*, 2022) and could indicate fault complexity or the presence of a blind thrust at depth. The main fault rupture consisted of dip-slip motion in the east and left-lateral strike-slip motion in the west (Calais *et al.*, 2022; Okuwaki and Fan, 2022), similar to the 2010 pattern of rupture on the Léogane fault (Calais *et al.*, 2010). This produced a pattern of uplift between the EPGF and the secondary fault

structures that is consistent with the implied direction of motion from the phase gradient and corresponding LoS deformation maps. The involvement of secondary faults in this rupture requires adjustments to the model of a simple segmented strike-slip EPGF (Saint Fleur *et al.*, 2020) and indicates that an accurate description of hazard should include transpression in a zone surrounding the main EPGF.

Locations with tropical climates and dense vegetation such as Haiti present a challenge for measuring surface deformation with InSAR. The longer wavelength of ALOS-2 data complemented by the frequent acquisitions of Sentinel-1 was a key pairing for the success of this study. The ability to resolve small-scale deformation features with phase gradient processing using L-band data in such a vegetated area is an important advance for the broader application of this technique. Sentinel-1 wrapped phase gradients have been successfully used to detect slip on secondary fault features in arid climates, that is, Ridgecrest in the Owens Valley (Xu, Sandwell, and Smith-Konter, 2020; Xu, Sandwell, Ward, et al., 2020), Landers (Price and Sandwell, 1998), and Hector Mine (Sandwell et al., 2000) in the eastern California shear zone in the Mojave desert. However, this work presents the first successful application in a vegetated region, which opens the door to future studies of a larger number of events in a wider variety of climates. In contrast to the previous studies, the Sentinel-1 phase gradients over Haiti were largely unable to resolve deformation features, even when stacking multiple pairs. The upcoming NASA-ISRO SAR (NISAR) mission should provide an ideal balance between frequent acquisitions and long wavelength (L-band) radar observations (Rosen and Kumar, 2021).

DATA AND RESOURCES

Aftershock locations were calculated by the local Haitian seismic network, Ayiti-Séismes (https://ayiti.unice.fr/ayiti-seismes/, last accessed May 2022) and Calais et al. (2022). Sentinel-1 Interferometric Synthetic Aperture Radar (InSAR) data used in this study were collected and distributed by the European Space Agency (ESA) and are freely available via the Sentinel data hub (http://scihub.copernicus.eu/ dhus, last accessed March 2022). Advanced Land Observation Satellite (ALOS)-2 InSAR data used in this study were collected by the Japanese Aerospace Exploration Agency (JAXA) and made available to the authors under an individual proposal. All interferograms and derived data products used in this study are made freely and publicly available at doi: 10.5281/zenodo.6834534 (Yin et al., 2022, last accessed October 2022) and also at https://topex.ucsd.edu/haiti_7.2/ index.html (last accessed September 2022). The supplemental material includes three supplemental figures and a more complete description of the moment deficit calculation referenced in the Discussion section. Figure S1 shows all Sentinel-1 wrapped phase interferograms during the 14 August-4 September 2021 time period in sequential pairs. Figure S2 shows the stacked phase gradient plot for ALOS-2 tracks A043 and A042 in the range (look) direction. Figure S3 shows an example of a phase gradient data from Sentinel-1 interferograms that do not show discernible deformation features.

DECLARATION OF COMPETING INTERESTS

The authors acknowledge that there are no conflicts of interest recorded.

ACKNOWLEDGMENTS

The authors are grateful to two reviewers, Qi Ou and Jeremy Maurer, for their thoughtful and constructive feedback which improved the article and figures. The authors thank the operators and hosts of the Ayiti-Séismes earthquake monitoring network at Bureau des Mines, Faculté des Sciences, Laboratoire URGéo, Université d'état d'Haïti, Ecole Normale Supérieur, and Laboratoire Géoazur for providing aftershock locations, and making them free and openly available. The authors thank European Space Agency (ESA) for the rapid acquisition and distribution of Sentinel-1 data. The authors thank Japanese Aerospace Exploration Agency (JAXA) for access to Advanced Land Observation Satellite (ALOS)-1 and ALOS-2 data. Rapid Interferometric Synthetic Aperture Radar (InSAR) data processing was supported by a National Science Foundation RAPID Grant (Number 2150704). The authors thank Sylvert Paul and Francoise Courboulex at GéoAzur, and Eric Calais at ENS for helpful discussions related to the earthquake. The authors thank Katherine Guns for InSAR processing support. The development of the GMTSAR software was supported by the National Science Foundation (NSF) through the NSF Office of Advanced Cyberinfrastructure program (Grant Number OAC-1834807), and the NSF EarthScope program (Grant Numbers EAR-1147435, EAR-1424374, and EAR-1614875). We acknowledge support from the National Aeronautics and Space Administration (NASA) through the Earth Surface and Interior program (Grant Numbers NNX16AK93G and 80NSSC19K1043), and NSF (Grant Number OAC-1835372).

REFERENCES

Aagaard, B. T., M. G. Knepley, and C. A. Williams (2013). A domain decomposition approach to implementing fault slip in finite-element models of quasi-static and dynamic crustal deformation, *J. Geophys. Res.* **118**, no. 6, 3059–3079, doi: 10.1002/jgrb.50217.

Aiken, C., K. Chao, H. Gonzalez-Huizar, R. Douilly, Z. Peng, A. Deschamps, E. Calais, and J. S. Haase (2016). Exploration of remote triggering: A survey of multiple fault structures in Haiti, *Earth Planet. Sci. Lett.* 455, 14–24, doi: 10.1016/j.epsl.2016.09.023.

Ali, S. T., A. M. Freed, E. Calais, D. M. Manaker, and W. R. McCann (2008). Coulomb stress evolution in northeastern Caribbean over the past 250 years due to coseismic, postseismic and interseismic deformation, *Geophys. J. Int.* **174**, no. 3, 904–918, doi: 10.1111/j.1365-246X.2008.03634.x.

Bien-Aime-Momplaisir, R., H. Amilcar, G. Murat-Pierre, and H. Cenatus-Amilcar (1988). *Geologic Map of Haiti (Carte géologique de la République d'Haïti)*, Bureau des Mines et de l'Energie (BME), Port-au-Prince, Haiti (in French).

Bodin, P., R. Bilham, J. Behr, J. Gomberg, and K. W. Hudnut (1994). Slip triggered on southern California faults by the 1992 Joshua tree, Landers, and big bear earthquakes, *Bull. Seismol. Soc. Am.* **83**, no. 3, 806–816.

Boisson, D. (1987). Etude geologique du massif du nord d'haiti (Hispaniola—grandes antilles), *Ph.D. Thesis*, available at http://www.theses.fr/1987PA066771 (in French).

- Calais, E., A. Freed, G. Mattioli, F. Amelung, S. Jönsson, P. Jansma, S. H. Hong, T. Dixon, C. Prépetit, and R. Momplaisir (2010).
 Transpressional rupture of an unmapped fault during the 2010 Haiti earthquake, *Nature Geosci.* 3, no. 11, 794–799, doi: 10.1038/ngeo992.
- Calais, E., S. Symithe, B. Mercier de Lepinay, and C. Prepetit (2016). Plate boundary segmentation in the northeastern Caribbean from geodetic measurements and Neogene geological observations, *C.R. Geosci.* **348**, no. 1, 42–51, doi: 10.1016/j.crte.2015.10.007.
- Calais, E., S. Symithe, T. Monfret, B. Delouis, A. Lomax, F. Courboulex, J. P. Ampuero, P. E. Lara, Q. Bletery, J. Chèze, et al. (2022). Citizen seismology helps decipher the 2021 Haiti earthquake, Science 376, no. 6590, 283–287, doi: 10.1126/science.abn1045.
- Chen, C. W., and H. A. Zebker (2002). Phase unwrapping for large SAR interferograms: Statistical segmentation and generalized network models, *IEEE Trans. Geosci. Remote Sens.* 40, no. 8, 1709–1719.
- Crameri, F., G. E. Shephard, and P. J. Heron (2020). The misuse of colour in science communication, *Nat. Commun.* 11, no. 1, 5444, doi: 10.1038/s41467-020-19160-7.
- DeMets, C., P. E. Jansma, G. S. Mattioli, T. H. Dixon, F. Farina, R. Bilham, E. Calais, and P. Mann (2000). GPS geodetic constraints on Caribbean-North America plate motion, *Geophys. Res. Lett.* **27**, no. 3, 437–440, doi: 10.1029/1999GL005436.
- Douilly, R., H. Aochi, E. Calais, and A. M. Freed (2015). Threedimensional dynamic rupture simulations across interacting faults: The M w 7.0, 2010, Haiti earthquake, *J. Geophys. Res.* **120**, no. 2, 1108–1128, doi: 10.1002/2014JB011595.
- Douilly, R., J. S. Haase, W. L. Ellsworth, M.-P. Bouin, E. Calais, S. J. Symithe, J. G. Armbruster, B. M. de Lépinay, A. Deschamps, S. L. Mildor, et al. (2013). Crustal structure and fault geometry of the 2010 Haiti earthquake from temporary seismometer deployments, Bull. Seismol. Soc. Am. 103, no. 4, 2305–2325, doi: 10.1785/0120120303.
- Douilly, R., S. Paul, T. Monfret, A. Deschamps, D. Ambrois, S. J. Symithe, S. St Fleur, F. Courboulex, E. Calais, D. Boisson et al. (2022). Rupture segmentation of the August 14, 2021 Mw7.2 Nippes, Haiti, earthquake using aftershock relocation from a local seismic deployment, Bull. Seismol. Soc. Am. 1–15, doi: 10.1785/0120220128.
- Frankel, A., S. Harmsen, C. Mueller, E. Calais, and J. Haase (2011). Seismic hazard maps for Haiti, *Earthq. Spectra* **27**, 23–41, doi: 10.1193/1.3631016.
- Hashimoto, M., Y. Fukushima, and Y. Fukahata (2011). Fan-delta uplift and mountain subsidence during the Haiti 2010 earthquake, *Nature Geosci.* **4**, no. 4, 255–259, doi: 10.1038/ngeo1115.
- Hayes, G. P., R. W. Briggs, A. Sladen, E. J. Fielding, C. Prentice, K. Hudnut, P. Mann, F. W. Taylor, A. J. Crone, R. Gold, et al. (2010). Complex rupture during the 12 January 2010 Haiti earth-quake, *Nature Geosci.* 3, no. 11, 800–805, doi: 10.1038/ngeo977.
- Hussain, E., T. J. Wright, R. J. Walters, D. Bekaert, A. Hooper, and G. A. Houseman (2016). Geodetic observations of postseismic creep in the decade after the 1999 Izmit earthquake, Turkey: Implications for a shallow slip deficit, *J. Geophys. Res.* 121, no. 4, 2980–3001, doi: 10.1002/2015JB012737.
- Jiang, J., Y. Bock, and E. Klein (2021). Coevolving early afterslip and aftershock signatures of a San Andreas fault rupture, *Sci. Adv.* 7, no. 15, eabc1606, doi: 10.1126/sciadv.abc1606.

- Johanson, I. A. (2006). Coseismic and postseismic slip of the 2004 Parkfield earthquake from space-geodetic data, *Bull. Seismol.* Soc. Am. 96, no. 4B, S269–S282, doi: 10.1785/0120050818.
- Langbein, J. (2006). Coseismic and initial postseismic deformation from the 2004 Parkfield, California, earthquake, observed by global positioning system, electronic distance meter, creepmeters, and borehole strainmeters, *Bull. Seismol. Soc. Am.* **96**, no. 4B, S304– S320, doi: 10.1785/0120050823.
- Li, Y., and R. Burgmann (2021). Partial coupling and earthquake potential along the Xianshuihe fault, China, *J. Geophys. Res.* **126,** no. 7, doi: 10.1029/2020JB021406.
- Mann, P., E. Calais, J.-C. Ruegg, C. DeMets, P. E. Jansma, and S. Mattioli (2002). Oblique collision in the northeastern Caribbean from GPS measurements and geological observations: Oblique collision in the northeastern Caribbean, *Tectonics* **21**, no. 6, 7-1–7-26, doi: 10.1029/2001TC001304.
- Mann, P., F. Taylor, R. Edwards, and T.-L. Ku (1995). Actively evolving microplate formation by oblique collision and sideways motion along strike-slip faults: An example from the northeastern Caribbean plate margin, *Tectonophysics* **246**, nos. 1/3, doi: 10.1016/0040-1951(94)00268-E.
- Maurer, J., R. Dutta, A. Vernon, and S. Vajedian (2022). Complex rupture and triggered aseismic creep during the August 14, 2021 Haiti earthquake from satellite geodesy (preprint), *Geodesy* doi: 10.1002/essoar.10510731.1.
- McCann, W. R. (2006). Estimating the threat of tsunamigenic earth-quakes and earthquake induced-landslide tsunami in the Caribbean, in *Caribbean Tsunami Hazard*, 43–65, doi: 10.1142/9789812774613 0002.
- Meng, L., J.-P. Ampuero, A. Sladen, and H. Rendon (2012). High-resolution backprojection at regional distance: Application to the Haiti M7.0 earthquake and comparisons with finite source studies, *J. Geophys. Res.* **117**, no. B4, doi: 10.1029/2011JB008702.
- Mercier de Lepinay, B., A. Deschamps, F. Klingelhoefer, Y. Mazabraud, B. Delouis, V. Clouard, Y. Hello, J. Crozon, B. Marcaillou, D. Graindorge, et al. (2011). The 2010 Haiti earthquake: A complex fault pattern constrained by seismologic and tectonic observations: The 2010 Haiti earthquake fault pattern, Geophys. Res. Lett. 38, no. 22, doi: 10.1029/2011GL049799.
- Okuwaki, R., and W. Fan (2022). Oblique convergence causes both thrust and strike-slip ruptures during the 2021 M 7.2 Haiti earthquake, *Geophys. Res. Lett.* **49**, no. 2, doi: 10.1029/2021GL096373.
- Prentice, C. S., P. Mann, A. J. Crone, R. D. Gold, K. W. Hudnut, R. W. Briggs, and P. Jean (2010). Seismic hazard of the Enriquillo-Plantain Garden fault in Haiti inferred from palaeoseismology, *Nature Geosci.* 3, no. 11, 789–793, doi: 10.1038/ngeo991.
- Price, E. J., and D. T. Sandwell (1998). Small-scale deformations associated with the 1992 Landers, California, earthquake mapped by synthetic aperture radar interferometry phase gradients, *J. Geophys. Res.* **103**, no. B11, 27,001–27,016, doi: 10.1029/98JB01821.
- Rosen, P. A., and R. Kumar (2021). NASA-ISRO SAR (NISAR) mission status, in 2021 IEEE Radar Conference (RadarConf21), IEEE, Atlanta, Georgia, U.S.A., doi: 10.1109/RadarConf2147009.2021.9455211.
- Saint Fleur, N., N. Feuillet, R. Grandin, E. Jacques, J. Weil-Accardo, and Y. Klinger (2015). Seismotectonics of southern Haiti: A new

- faulting model for the 12 January 2010 M 7.0 earthquake, *Geophys. Res. Lett.* **42,** doi: 10.1002/2015GL065505.
- Saint Fleur, N., Y. Klinger, and N. Feuillet (2020). Detailed map, displacement, paleoseismology, and segmentation of the Enriquillo-Plantain Garden fault in Haiti, *Tectonophysics* 778, doi: 10.1016/j.tecto.2020.228368.
- Sandwell, D. T., and E. J. Price (1998). Phase gradient approach to stacking interferograms, *J. Geophys. Res.* **103**, no. B12, 30,183–30,204, doi: 10.1029/1998JB900008.
- Sandwell, D. T., R. Mellors, X. Tong, M. Wei, and P. Wessel (2011). GMTSAR: An InSAR processing system based on generic mapping tools, *Tech. Rept. Nos. LLNL-TR-481284*, 1090004, doi: 10.2172/ 1090004.
- Sandwell, D. T., L. Sichoix, D. Agnew, Y. Bock, and J.-B. Minster (2000). Near real-time radar interferometry of the Mw 7.1 Hector mine earthquake, *Geophys. Res. Lett.* **27**, no. 19, 3101–3104, doi: 10.1029/1999GL011209.
- Shanker, A., and H. Zebker (2009). Sparse two-dimensional phase unwrapping using regular grid methods, *IEEE Geosci. Remote Sens. Lett.* **6**, no. 3, 519–522, doi: 10.1109/LGRS.2009.2020522.
- Symithe, S. J., and E. Calais (2016). Present-day shortening in Southern Haiti from GPS measurements and implications for seismic hazard, *Tectonophysics* **679**, 117–124, doi: 10.1016/j.tecto.2016.04.034.
- Symithe, S. J., E. Calais, J. B. de Chabalier, R. Robertson, and M. Higgins (2015). Current block motions and strain accumulation on active faults in the Caribbean: Current Caribbean kinematics, *J. Geophys. Res.* **120**, no. 5, 3748–3774, doi: 10.1002/2014JB011779.
- Symithe, S. J., E. Calais, J. S. Haase, A. M. Freed, and R. Douilly (2013). Coseismic slip distribution of the 2010 M 7.0 Haiti earthquake and resulting stress changes on regional faults, *Bull. Seismol. Soc. Am.* **103**, no. 4, 2326–2343, doi: 10.1785/0120120306.
- Tymofyeyeva, E., Y. Fialko, J. Jiang, X. Xu, D. Sandwell, R. Bilham, T. K. Rockwell, C. Blanton, F. Burkett, A. Gontz, *et al.* (2019). Slow slip event on the southern San Andreas fault triggered by the 2017 Mw 8.2 Chiapas (Mexico) earthquake, *J. Geophys. Res.* 124, no. 9, 9956–9975, doi: 10.1029/2018JB016765.
- U.S. Geological Survey (USGS) (2021). M 7.2—Nippes, Haiti, available at https://earthquake.usgs.gov/earthquakes/eventpage/us6000f65h/executive (last accessed February 2022).

- Wang, J., P. Mann, and R. R. Stewart (2018). Late Holocene structural style and seismicity of highly transpressional faults in southern Haiti, *Tectonics* **37**, no. 10, 3834–3852, doi: 10.1029/2017TC004920.
- Wdowinski, S., and S.-H. Hong (2011). Postseismic deformation following the 2010 Haiti earthquake: Time-dependent surface subsidence induced by groundwater flow in response to a sudden uplift, Fringe 697, 5.
- Wei, S., E. Fielding, S. Leprince, A. Sladen, J.-P. Avouac, D. Helmberger, and R. Briggs (2011). Superficial simplicity of the 2010 El Mayor-Cucapah earthquake of Baja California in Mexico, *Nature Geosci.* 4, no. 9, 615–618, doi: 10.1038/ngeo1213.
- Wessel, P., J. F. Luis, L. Uieda, R. Scharroo, F. Wobbe, W. H. F. Smith, and D. Tian (2013). The generic mapping tools version 6, Geochem. Geophys. Geosys. doi: 10.1029/2019GC008515.
- Wessels, R. J., N. Ellouz-Zimmermann, N. Bellahsen, Y. Hamon, C.
 Rosenberg, R. Deschamps, R. Momplaisir, D. Boisson, and S. Leroy (2019). Polyphase tectonic history of the southern Peninsula, Haiti:
 From folding-and-thrusting to transpressive strike-slip,
 Tectonophysics 751, 125–149, doi: 10.1016/j.tecto.2018.12.011.
- Xu, X., D. T. Sandwell, and B. Smith-Konter (2020). Coseismic displacements and surface fractures from Sentinel-1 InSAR: 2019 Ridgecrest earthquakes, Seismol. Res. Lett. 91, no. 4, 1979– 1985, doi: 10.1785/0220190275.
- Xu, X., D. T. Sandwell, E. Tymofyeyeva, A. González-Ortega, and X. Tong (2017). Tectonic and anthropogenic deformation at the Cerro Prieto geothermal step-over revealed by Sentinel-1A InSAR, *IEEE Trans. Geosci. Remote Sens.* 55, no. 9, 5284–5292.
- Xu, X., D. T. Sandwell, L. A. Ward, C. W. D. Milliner, B. R. Smith-Konter, P. Fang, and Y. Bock (2020). Surface deformation associated with fractures near the 2019 Ridgecrest earthquake sequence, *Science* 370, no. 6516, 605–608, doi: 10.1126/science.abd1690.
- Yin, H. Z., X. Xu, J. S. Haase, R. Douilly, D. T. Sandwell, and B. Mercier de Lépinay (2022). InSAR interferograms and products from 2021, M7.2 Nippes, Haiti earthquake (curated dataset), Zenodo, doi: 10.5281/zenodo.6834534.

Manuscript received 16 June 2022 Published online 28 October 2022